Ann. Phys. (Berlin) **528**, No. 9–10, 677–683 (2016) / DOI 10.1002/andp.201600103

annalen der physik

Large circular dichroism and optical rotation in titanium doped chiral silver nanorods

Jitto Titus[1], *George Larsen*[2], *Yiping Zhao*[2], *and A. G. Unil Perera*[1,*]

Received 14 April 2016, revised 10 June 2016, accepted 29 June 2016
Published online 29 July 2016

The circular dichroism of titanium-doped silver chiral nanorod arrays grown using the glancing angle deposition (GLAD) method is investigated in the visible and near infrared ranges using transmission ellipsometry and spectroscopy. These films are found to have significant circular polarization effects across broad ranges of the visible to NIR spectrum, including large values for optical rotation. The characteristics of these circular polarization effects are strongly influenced by the morphology of the deposited arrays. Thus, the morphological control of the optical activity in these nanostructures demonstrates significant optimization capability of the GLAD technique for fabricating chiral plasmonic materials.

1 Introduction

Chiral metamaterials [1, 2] have the ability to rotate the plane of polarization of electromagnetic waves while minimally absorbing the light. These chiral metamaterials also selectively transmit left or right circular polarized light. The significance of these optically active metamaterials have increased since the prediction of phenomena such as negative refraction and negative reflection [3]. Moreover, they find diverse applications like differentiating enantiomers in analytical chemistry [4], identifying protein conformations in life sciences [5], bio-weapon [6] and missile detection [7] in defense, etc.

Glancing Angle Deposition [8] (GLAD) is a vapor deposition technique that proves to be a simple yet scalable method which can be used to fabricate arrays of plasmonic nanostructures [9, 10]. Silver has the lowest damping rate, taking into account the scattering due to electron-electron and electron-phonon interactions and lattice defects. Of all the known metal or metal-like materials, in the visible and near infrared region, silver is one of the best candidates for plasmonic devices [11]. Silver, and noble metals in general, are difficult to use with the GLAD technique due to the high mobilities of surface adatoms, making it difficult to sculpt the materials into asymmetric shapes necessary for chiral metamaterials. However, several techniques have recently been developed that enable the fabrication of chiral noble metal nanostructures using GLAD. [12–15] Of these, titanium-doped Ag helices are particularly interesting, as they are among the simplest to fabricate and their morphological properties are easily tuned. [16] Furthermore, they exhibit intense circular dichroism in the visible region. While the results for the visible region are impressive, characterization of the chiral optical properties of the Ti-doped Ag helices is incomplete, especially in the near-infrared wavelength regions that are important for telecom and biomedical applications. This report investigates the optical properties of Ti-doped Ag helices in the visible and near infrared ranges using transmission ellipsometry and spectroscopy.

2 Experimental section

The morphological control of the optical activity in these nanostructures demonstrates the significant optimization capability of the GLAD technique. Silver chiral nanorod structures [16] (CNS) have been grown using a dynamic shadowing growth method, a type of GLAD technique which is further explained elsewhere [8]. In this method, quartz substrates were mounted inside a vacuum deposition chamber on six independently rotating holders, where each holder rotates azimuthally at different speeds, producing six sets of chiral nanorods with different morphological parameters. These samples are labeled, CNS 1 – 6, where CNS 1 rotates the fastest

* Corresponding author E-mail: uperera@gsu.edu
[1] Department of Physics and Astronomy, Optoelectronics Laboratory, GSU, Atlanta, GA
[2] Department of Physics and Astronomy, Nanolab, UGA, Athens, GA

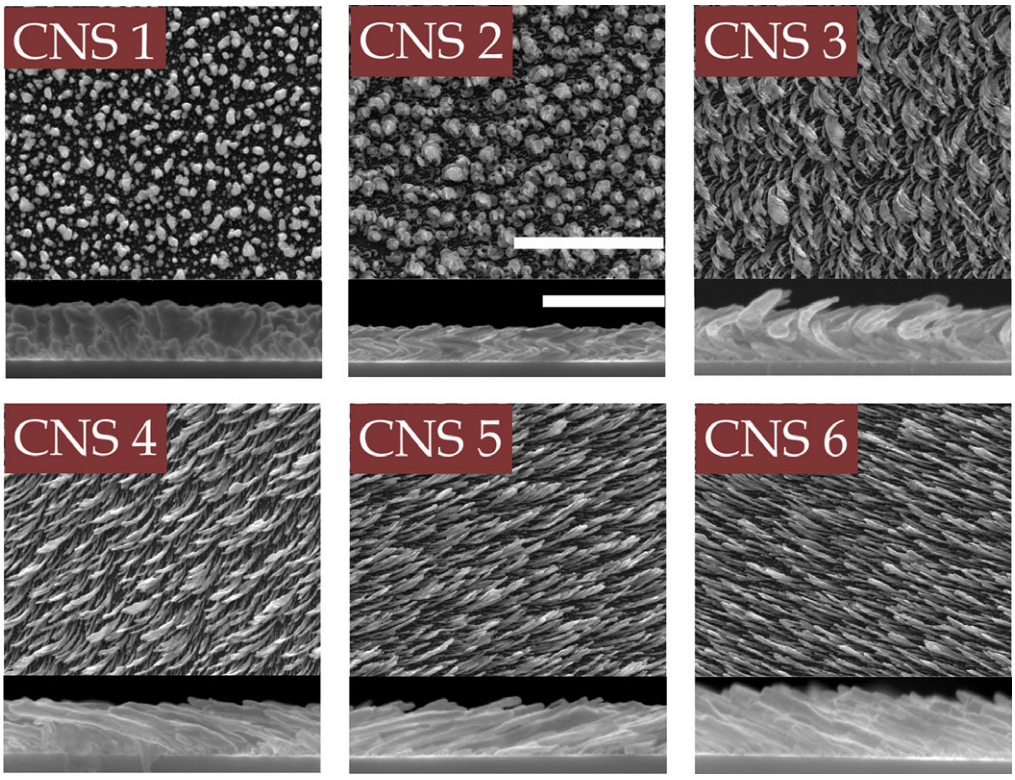

Figure 1 Scanning electron microscope images of Ag:Ti composite chiral nanorod structures CNS 1 to 6. In each of the six images, the upper portion represents the top view and the lower portion, the cross sectional side view of the samples. The scale bars in the top and side views are 2 μm and 500 nm.

and CNS 6 rotates the slowest. The rotation direction also alternates, CNS 1, 3 and 5 rotated in a clockwise manner throughout the deposition, while CNS 2, 4 and 6 rotated in a counter-clockwise manner. The Ag:Ti vapor flux, obtained by dual-source electron beam evaporation, is made to be incident on these substrates at a large angle (~87°) with respect to the incident flux, where the vapor incident angle is accomplished by tilting the substrate holder. The vapor flux is maintained at a nominal 5% volume ratio of Ti to Ag throughout the deposition process, and each of the fluxes are monitored by separate quartz crystal microbalances. Due to slightly different positions within the chamber, there are slight differences in the Ti/Ag ratios at each of the holders, but these differences are less than ±5% of the Ti/Ag ratio for holder number 3. The nominal five percent Ti atoms used in the vapor mix serves as a barrier to prevent the surface diffusion of silver adatoms, and therefore allows for the sculpting of chiral nanorod arrays. Scanning electron microcopy images of samples CNS 1 to 6 are shown in Fig. 1 with both top and cross-sectional side views. As is evident from the images, the dimensional parameters of the samples such as density, radius of curvature, height, pitch and the diameter of nanorod, vary with respect to the speed of rotation of the sample stages.

The measured average values of these morphological parameters for the CNS samples are listed in Table 1. In general, the samples change from post-like structures (CNS 1) to full helices (CNS 2) to partial helices (CNS 3 – 6) as the substrate rotation speed decreases. In other words, the radius of curvature of the chiral structure is indirectly proportional to the speed of the sample rotation with CNS 1 having the smallest to CNS 6 having the largest radius of curvature. On the other hand, the pitch of the samples increases as the rotation speed decreases, as expected. The density or the packing factor of the nanorods, as measured through SEM analysis, do not vary greatly except for samples CNS 1 and CNS 2 as there are more bifurcations and coalescing of the nanorods. Overall, the morphology is consistent with growth processes where there is competition between surface diffusion and atomic shadowing [17]. The absorbance spectra of the CNS samples (obtained using J. A Woolam M-2000 ellipsometer) as seen in Fig. 2 indicate that the CNS samples with faster rotation speeds (CNS1, CNS2 and CNS3) have stronger local surface plasmon resonance

Table 1 Morphological parameters of the chiral nanorod samples that vary with the sample stage rotation rate. The pitch and radius of curvature increases from CNS 1 to 6 as the sample rotation rate decreases.

	Height (nm)	Diameter (nm)	Density (1/μm^2)	Radius of Curvature (nm)	Pitch (nm)
CNS 1 (fastest rotation rate)	160 ± 60	N/A	52	N/A	N/A
CNS 2	110 ± 30	30 ± 10	37	90 ± 20	100 ± 5
CNS 3	240 ± 20	50 ± 30	18	260 ± 30	560 ± 50
CNS 4	200 ± 50	40 ± 10	13	540 ± 20	900 ± 200
CNS 5	200 ± 20	50 ± 20	19	1120 ± 90	1900 ± 200
CNS 6 (slowest rotation rate)	220 ± 20	40 ± 10	18	2000 ± 200	4200 ± 400

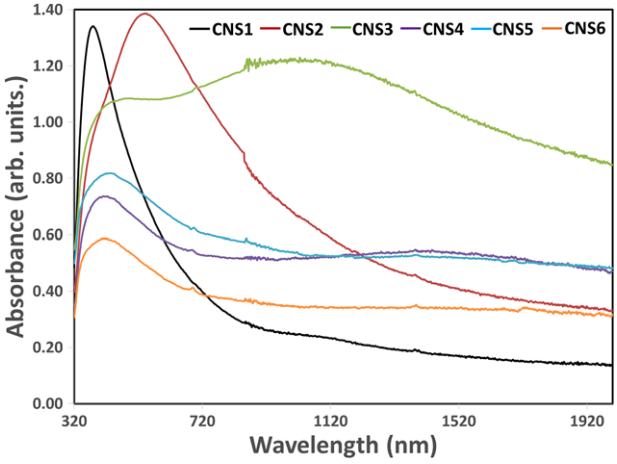

Figure 2 Absorbance spectra CNS samples indicating stronger local palsmon resonance absorbances in samples with faster growth rotation speeds (CNS1, CNS2 and CNS3) than those with slower growth rotation speeds (CNS4, CNS5 and CNS6).

absorption modes than the samples with slower rotation speeds (CNS4, CNS5 and CNS6). The absorbances are averaged for each sample by rotating the sample azimuthally.

Circular dichroism measurements were done using transmission ellipsometry (J.A. Woollam M-2000, 370 – 1000 nm) for the visible region and FTIR spectroscopy (Bruker Vertex70, 900 – 2000 nm) for the NIR regions while averaging over different azimuthal orientations. Circularly polarized light obtained by sending light through a holographic KRS-5 wire grid linear polarizer (Thorlabs WP50H-K) followed by an achromatic broadband flat retardance (Thorlabs AQWP05M) quarter wave plate in the FTIR sample compartment is incident on the sample. Having the fast axis of the quarter wave plate at +45 and −45° to the linear polarizer produced right and left circularly polarized light respectively.

ORD measurements in the visible region were performed by passing unpolarized light through a Glan-calcite linear polarizer (Thorlabs GTH10M). The polarized light, on passing through the CNS sample undergoes a rotation of the plane of linear polarized light to various degrees depending on the radius of curvature and the pitch of the CNS samples. The light was then made to pass through an analyzer whose axis was orthogonal to the polarizer. The angle by which the analyzer had to be rotated to achieve a transmission minimum determined the optical activity of the CNS sample. An Ocean Optics (USB4000) and a Bruker Vertex 70 FTIR spectrometers are used to simultaneously obtain the minimum angles of rotation as a function of wavelength over the entire visible and NIR ranges.

3 Results and discussion

Circular dichroism was studied in these samples by employing transmission ellipsometry in the visible region and Fourier Transform Infrared (FTIR) spectroscopy in the near infrared (NIR) region. The transmittances of the CNS samples are determined for right and left circular polarized light separately for the NIR region. The Mueller index (m_{14}) can be measured directly using ellipsometry, and it can also be extracted from the FTIR measurements (Fig. 3) using the formula $m_{14} = (T_{\text{right}} - T_{\text{left}})/2$, where, T_{right} and T_{left} are the transmittances of right and left circular polarized light respectively through the CNS samples (Fig. 4). Note that both ellipsometry and FTIR measurements only measure transmitted light, and therefore, light that is either absorbed or scattered does not contribute to the m_{14} spectra. The Mueller indices in the NIR

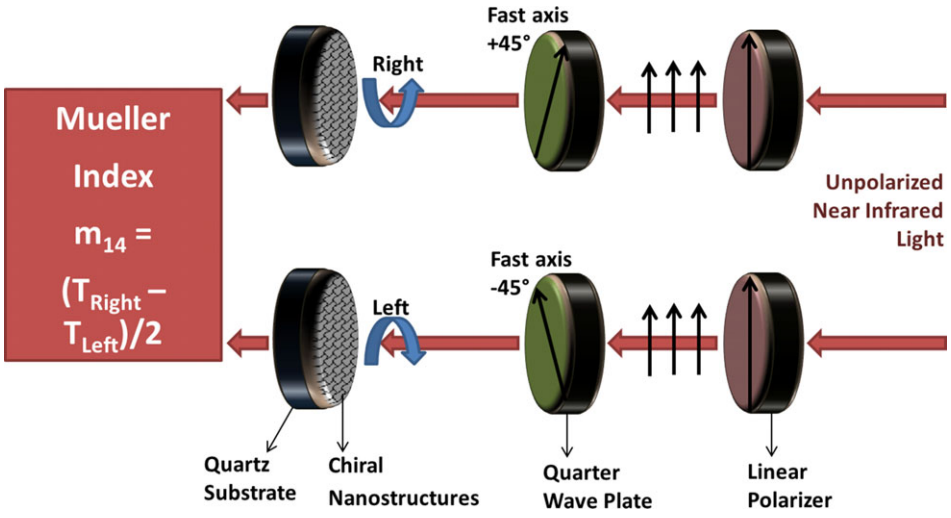

Figure 3 Schematic of the experimental design to determine the Mueller index from the transmittances of the left and right circular polarized light through the sample.

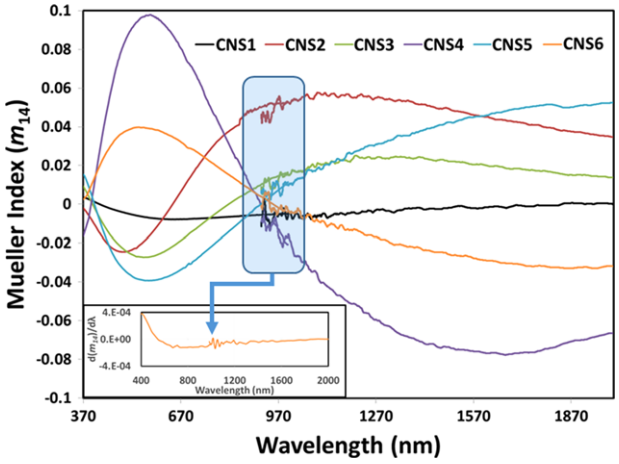

Figure 4 Mueller index extracted from ellipsometry (visible) and FTIR (NIR) transmittances for CNS samples. The samples show a bisignate response with CNS 4 showing the highest circular dichroism at ~570 nm. The rectangular box indicates the overlapping wavelength ranges. The NIR responses were individually offset by adding a DC value to merge with the visible responses. The inset shows the first derivative of the Mueller index for sample CNS6 indicating a good overlap of the visible and NIR regions without the need for offsetting, thus confirming the DC nature of the offset.

region required individual DC offsets to match the visible data. The inset in Fig. 3 shows the first derivative of m_{14} for samples CNS 3 and CNS 6 as examples where there is a smooth overlap between the visible and NIR regions without the need for offseting indicating the DC nature of the offset.

The Mueller index (m_{14}) spectra are directly related to the circular dichroism spectra of the CNS samples, and it can be seen that the samples exhibit selective transmittance of circular polarized light over the entire measured region with a high degree of selectivity. The left or right handedness of the spectra alternate with the different substrate rotation directions of CNS 1 – 6, as would be expected, and the relative optical chirality scales with the chirality of the structure; *i.e.*, the post-like structures have much smaller circular polarization effects than the full and partial helices. In general, all of the spectra have a broad, bisignate response, where one peak is centered over the visible region and the other opposite peak is centered over the NIR. The visible and NIR peaks have roughly the same intensity in all CNS samples, but the NIR peak does red-shift more strongly than the visible peak for CNS samples with increasing radii of curvature. The most remarkable features of the spectra are the broad m_{14} peaks which are relatively flat over several hundred nanometers in the NIR range, making these films interesting candidates for optical components in that important wavelength region.

In our previous work, [16] we describe a computational finite-difference-time-domain (FDTD) model that captures this broadband optical response of the GLAD helical films. The model assumes that individual helices will couple with the incident light through plasmonic resonances, and the polarization sensitivity and energy at which these resonance occurs depends on their morphology. [18, 19] In general, the circular polarization sensitive resonances of the helices are similar to standing waves, where the lowest energy mode has zero nodes.

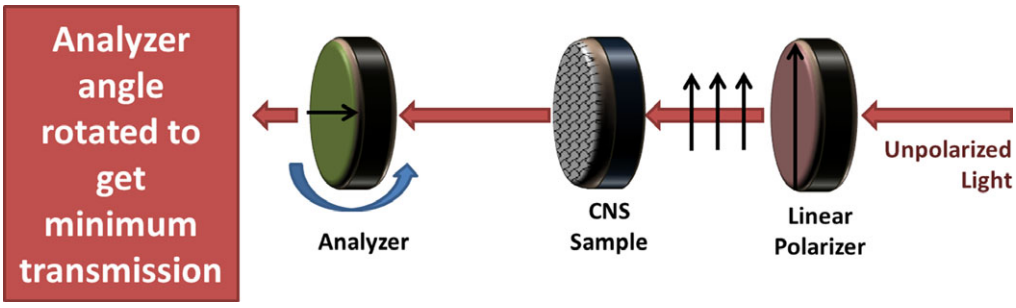

Figure 5 Experimental schematic to determine the angle of rotation of the linear polarization plane by the CNS samples. The sample is placed in a closed polariscope. The angle by which the sample has to be rotated to once again obtain minimum transmission indicates its optical activity.

The number of nodes increases in integer steps as the excitation energy of the resonances increases. As described above, the morphological parameters of the GLAD films are statistically variable, and therefore, the measured optical response of the film is actually an average response of slightly differently shaped chiral nanostructures. By using FDTD to simulate the individual chiral optical responses of helices having different parameters and then averaging these responses, the computational model was able to capture the broadband chiral optical signature of the GLAD helical films. In particular, the model averaged over the pitch number parameter because this parameter best captures the competitive mechanism of GLAD growth.

Since the CNS samples exhibit significant circular dichroism as described above, it indicates that the samples are also capable of rotating the plane of linear polarized light passing through them. In fact, the circular dichroism and optical rotation dispersion are related through the Kramers-Kronig relations [20]. To investigate the optical activity of the samples, an experiment was designed which is akin to a polarimeter setup with a slight modification to determine the angle of rotation (Fig. 5). Optical rotation dispersion is obtained by determining the minimum angle by which the CNS samples have to be rotated to obtain minimum transmission in the closed polariscope setup. According to the polarimetry measurements, the sample CNS 2 had the highest rotation angle of all samples at $-17°$ at ~620 nm, which is one of the largest optical rotations of linear polarization reported for thin film samples [21]. Since these structures are both chiral and linearly anisotropic, it may not be possible to completely separate the different contributions in the polarimetric measurements. For example, the experimentally determined orientations for linear polarization transmittance minima might actually result from both linear anisotropy and circular anisotropy since linear polarization can be described in a circular basis. However, the effect of linear birefringence property of the sample could be minimized by first rotating the sample with respect to the polarizer to maximize the throughput. This ensured that the polarizer's axis was parallel to the sample's apparent linear polarization axis. The analyzer is then introduced such that its axis is orthogonal to the polarizer's. The optical activity is then obtained by determining the smallest angle of analyzer rotation which will yield minimum throughput.

In order to get a different and wider range perspective of the optical rotation of the CNS samples, a numerical Kramers-Kronig (K-K) transformation based on the method by Ohta and Ishida has been applied to CD data obtained from the m_{14} spectra of the CNS samples over the visible and NIR wavelength regions. The experimentally obtained ORD values conformed well with the ORD obtained from K-K transformed Mueller index in the visible and NIR regions (Fig. 6), except for sample CNS3, the reasons for which are not clear yet. Individual DC offsets are applied to the polarimetric ORD data to show the conformity of the spectra. The good agreement between these spectra is a strong corroboration of the polarimetric experimental design. The results of the K-K transformed Mueller index for the entire visible and NIR region are plotted in Fig. 6. While an exact K-K transformation would require integration of all wavelengths and there appears to be some artifacts near the spectral endpoints, the obtained optical rotation spectra are consistent with what would be expected from the m_{14} measurements. That is, the mostly achiral film, CNS 1, does not exhibit significant optical rotation, and the opposite-handed films rotate linearly polarized light in opposite directions. According to the K-K transformations, CNS 2, which is the full helical structure, rotates light the most strongly of the CNS samples, with a large rotation angle of approximately $-17°$ at ~620 nm. In general, optical

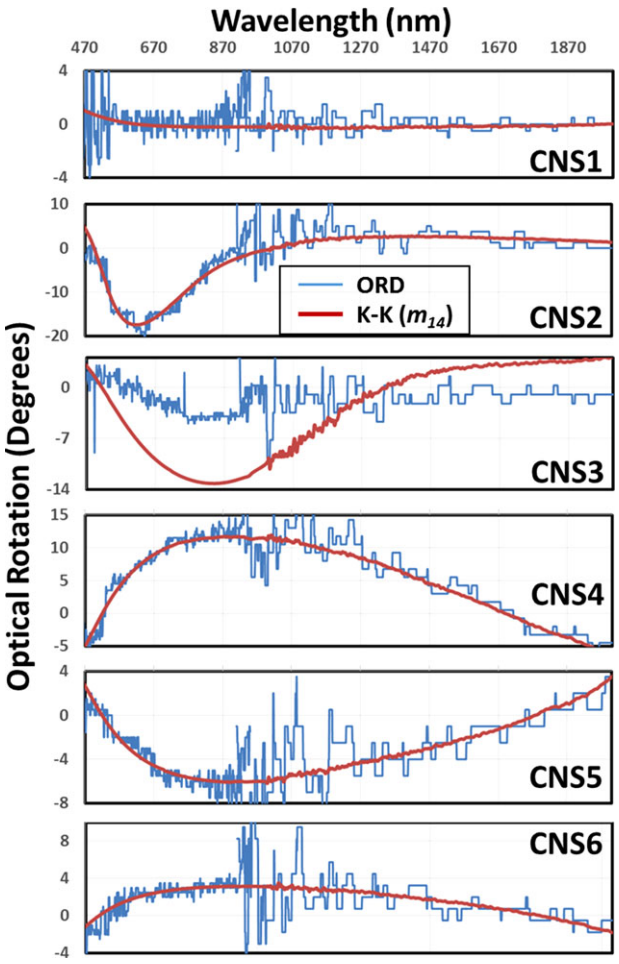

Figure 6 Optical rotation dispersion (ORD) angles as a function of wavelength for CNS samples. The ORD obtained by performing the Kramers Kronig transformation of the Mueller index (m_{14}) extracted from ellipsometry and FTIR spectroscopy is shown in red. Individual DC offsets are done to show the agreement between the optical rotation angles determined from the two experiments. The reason for the deviation of data for CNS3 is not known yet.

rotation spectra of the CNS films contain multiple peaks, with the peaks centered at wavelengths <1000 nm rotating light more strongly than the longer wavelength peaks. Another interesting result is that for the one turn helix ($N \approx 1$, CNS 2) and partial helices (pitch number, $N < 1$, CNS 3–6), the longer wavelength peak broadens as the pitch number decreases. The intensity of this peak also decreases as the pitch number decreases. A similar effect can be seen in the m_{14} spectra (Fig. 3) for the smaller wavelength peak, but the effect is more pronounced in the optical rotation spectra. Thus, for these helices there appears to be an inverse relationship between the width and intensity of optical rotation peaks.

4 Conclusion

Chiral nanorods grown using the scalable glancing angle deposition method with self-shadow masking technique were shown to be highly dichroic to circular polarized light with significantly high optical rotation of the plane of linear polarized light, where the specific polarization response could be controlled by the morphological parameters of the thin films. Notably, the observed optical activity of the CNS samples extended over wide regions of the visible and NIR spectrum. The ability to tune the optical activity over the visible and NIR regions by changing the morphological parameters of the CNS samples makes them promising candidates for plasmonic and nanophotonic substrates for biomedical and electro-optic device applications.

Acknowledgements. We would like to acknowledge the 'Molecular Basis of Diseases (MBD)' research program, US Army (W911 NF-15-1-0018) and support from the National Science Foundation (Grant No. ECCS-1029609 and CMMI-1435309) that made this research possible. Authors Jitto Titus and George Larsen contributed equally to this work.

Key words. metamaterial, chiral, dichroism, optical rotation, ftir spectroscopy.

References

[1] B. Wang, J. Zhou, T. Koschny, M. Kafesaki, and C. M. Soukoulis, Journal of Optics A: Pure and Applied Optics **11** 114003 (2009).
[2] S. Tretyakov, A. Sihvola, and L. Jylhä, Photonics and Nanostructures - Fundamentals and Applications **3** 107–115 (2005).
[3] J. Pendry, Science **306** 1353–1355 (2004).
[4] N. Purdie, and K. A. Swallows, Analytical chemistry **61** 77A-89A (1989).
[5] T. A. Keiderling, Current opinion in chemical biology **6** 682–688 (2002).
[6] D. Morrison, T. R. Austin, D. Ivnitski, and F. Milanovich, NATO Security through Science Series, Series B: Physics and Biophysics **1** (2005).
[7] T. Nee, and S. Nee, Shipboard Infrared Circular Polarization Sensor for Sea-Skimming Missile Detection, DTIC Document, (1999).
[8] Y. He, and Y. Zhao, Nanoscale **3** 2361–2375 (2011).
[9] J. D. Driskell, S. Shanmukh, Y. Liu, S. B. Chaney, X.-J. Tang, Y.-P. Zhao, and R. A. Dluhy, J. Phys. Chem. C **112** 895–901 (2008).
[10] Y. He, J. Fu, and Y. Zhao, Frontiers of Physics **9** 47–59 (2014).

[11] P. R. West, S. Ishii, G. V. Naik, N. K. Emani, and V. M. Shalaev, A. Boltasseva, Laser & Photonics Reviews **4** 795–808 (2010).
[12] A. G. Mark, J. G. Gibbs, T.-C. Lee, and P. Fischer, Nature materials **12** 802–807 (2013).
[13] J. H. Singh, G. Nair, A. Ghosh, and A. Ghosh, Nanoscale **5** 7224–7228 (2013).
[14] G. Larsen, Y. He, W. Ingram, E. LaPaquette, J. Wang, and Y.-P. Zhao, Nanoscale (2014).
[15] H. Johnson Singh, and A. Ghosh, The Journal of Physical Chemistry C **116** 19467–19471 (2012).
[16] G. K. Larsen, Y. He, J. Wang, and Y. Zhao, Advanced Optical Materials **2** 245–249 (2014).
[17] S. Mukherjee, and D. Gall, Thin Solid Films **527** 158–163 (2013).
[18] Z.-Y. Zhang, and Y.-P. Zhao, Appl. Phys. Lett. **90** 221501 (2007).
[19] J. K. Gansel, M. Wegener, S. Burger, and S. Linden, Opt. Express **18** 1059–1069 (2010).
[20] P. L. Polavarapu, The Journal of Physical Chemistry A **109** 7013–7023 (2005).
[21] D.-H. Kwon, P. L. Werner, and D. H. Werner, Opt. Express **16** 11802–11807 (2008).